Supporting Information

Achieving a higher lithium density in anode surpassing that of pure metallic lithium for high-energy-density batteries

Xiancheng Wang,[1,§] Bao Zhang,[2,§] Wenyu Wang,[1] Zihe Chen,[1] Shiyu Liu,[1] Shuibin Tu,[1] Renming Zhan,[1] Li Wang,[3] Yongming Sun,[1,*]

1 Wuhan National Laboratory for Optoelectronics, Huazhong University of Science and Technology, Wuhan 430074, China

2 School of Materials and Energy, University of Electronic Science and Technology of China, Chengdu 611731, China

3 Institute of Nuclear and New Energy Technology, Tsinghua University, Beijing 100084, China

§ These authors contributed equally to this work.
* Corresponding author

* E-mail: yongmingsun@hust.edu.cn

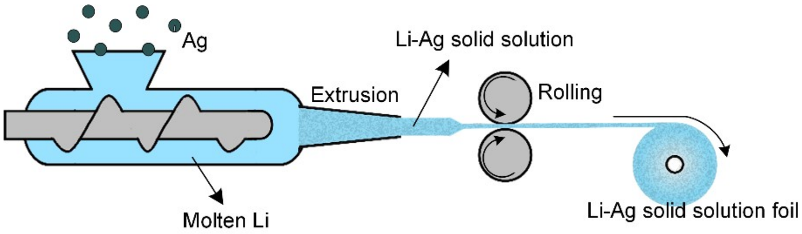

Figure S1. Schematic of the preparation process of the LixAg ($x = 6, 9, 12, 15, 18$) solid solution foil utilized the reaction between molten Li and Ag with certain stoichiometric ratio.

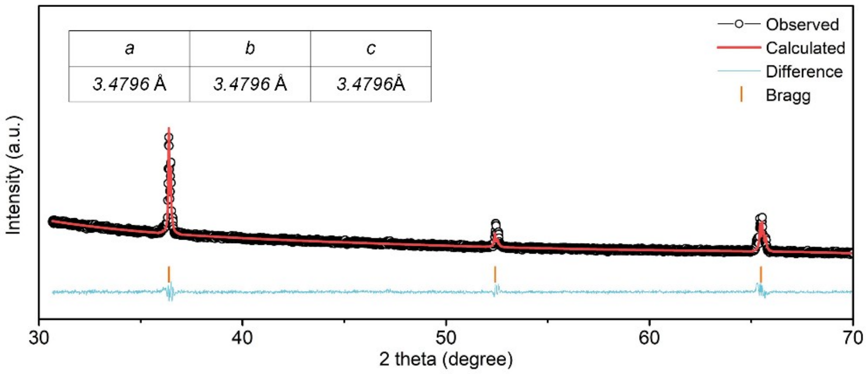

Figure S2. Rietveld refinement on XRD pattern of $Li_{15}Ag$.

The interaction between Li and Ag results in a continuous process of Li-Ag solid solution formation. As the Li content increases, the unit volume of Li undergoes alterations. This phenomenon also induces changes in lattice parameters and crystal structure. When a Li-rich Li-Ag solid solution is established, its crystal structure resembles that of pure Li (space group of Im-3m). However, due to Ag's smaller atomic radius compared to that of Li (1.44 Å vs. 1.52 Å), and the notable difference in electronegativity between these two elements (1.93 and 0.98, based on Pauling electronegativity scale), the Li lattice experiences a degree of contraction, leading to a reduction in unit cell size. Consequently, at a specific Li/Ag ratio, it is feasible for the Li content per unit volume to exceed that found in pure Li as a result of this decrease in unit cell dimensions. As the Li concentration within the Li-Ag solid solution continues to rise further, the impact of Ag on unit cell size becomes minimal. Thus, at this stage, the Li content per unit volume will again approximate that of pure Li.

Previous literature has reported some Li-Ag phases, demonstrating that the lattice parameters of Li-Ag are smaller than those of Li. For instance, Firth et al. reported that in a Li-Ag solid solution with an Ag content below 0.5 at%, the lattice parameter decreased by ~ 1.70 × 10^{-2} Å when the Ag concentration was increased by 1 at%[1]. Kellington et al reported a $Li_{0.98}Ag_{0.02}$ ($Li_{49}Ag$) phase showed a lattice parameters of 3.4913 Å ($a = b = c$)[2]. Besides, LiAg showed a lattice parameters of 3.174 Å ($a = b = c$, JCPDS#04-0805).

To provide a qualitative comparison, we conducted an analysis of the crystallographic information for the $Li_{15}Ag$ sample utilizing the Rietveld refinement method. The crystal structure and refined X-ray diffraction (XRD) pattern of $Li_{15}Ag$ are presented in Fig. S2, demonstrating that $Li_{15}Ag$ exhibits a typical cubic structure (space group of Im-3m, with lattice parameters $a = b = c$ =3.4796 Å), which is smaller than that of Li ($a = b = c$ =3.509 Å).

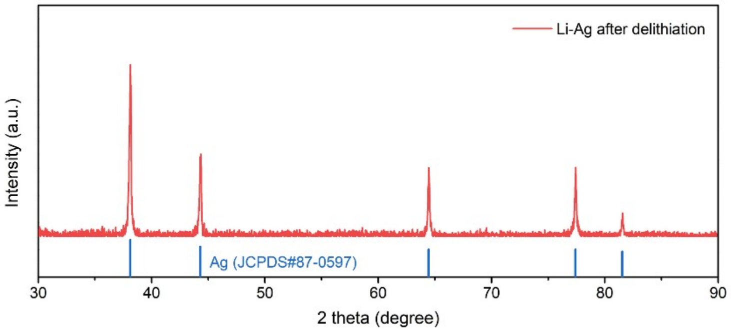

Figure S3. XRD patterns of the Li-Ag solid solution after complete delithiation to 1 V (vs. Li/Li^+) in a Li||Ag cell.

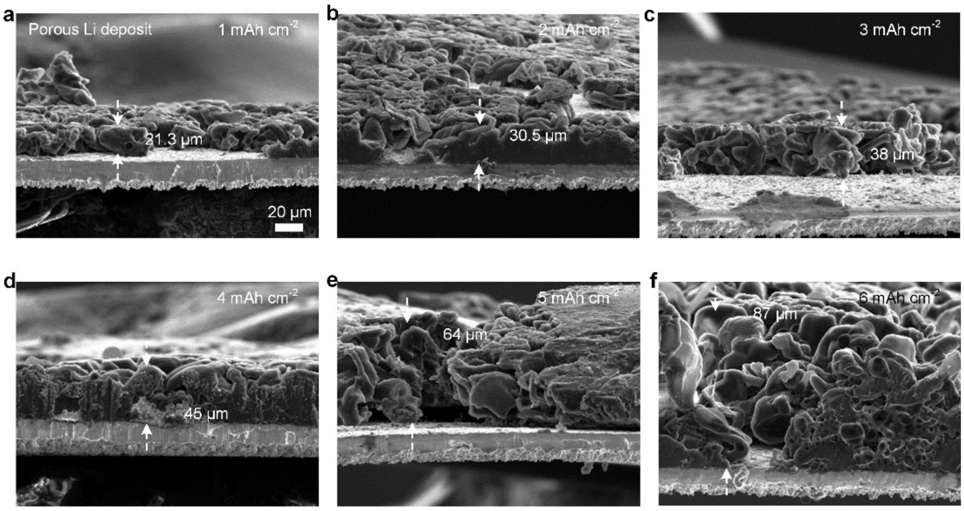

Figure S4. Cross-section SEM images of Li plating layers with capacities of (a) 1, (b) 2, (c) 3, (d) 4, (e) 5 and (f) 6 mAh cm^{-2}.

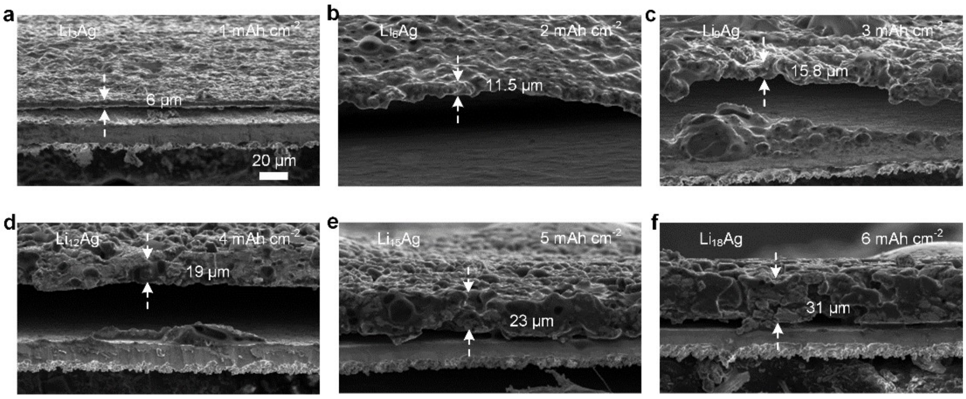

Figure S5. Cross-section scanning electron microscope (SEM) images of 1.3-μm Ag foil electrode after Li filling for (a) 1, (b) 2, (c) 3, (d) 4, (e) 5 and (f) 6 mAh cm^{-2} to form Li_3Ag, Li_6Ag, Li_9Ag, $Li_{12}Ag$, $Li_{15}Ag$, and $Li_{18}Ag$, respectively.

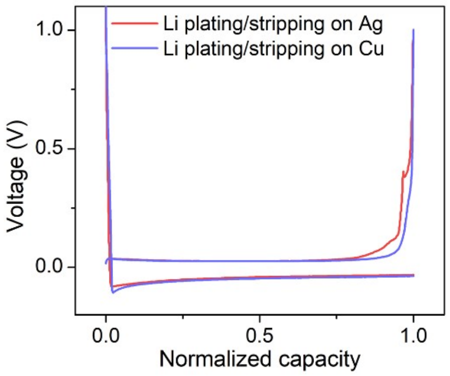

Figure S6. Initial electrochemical Li plating/stripping curves of Li||Ag and Li||Cu cells.

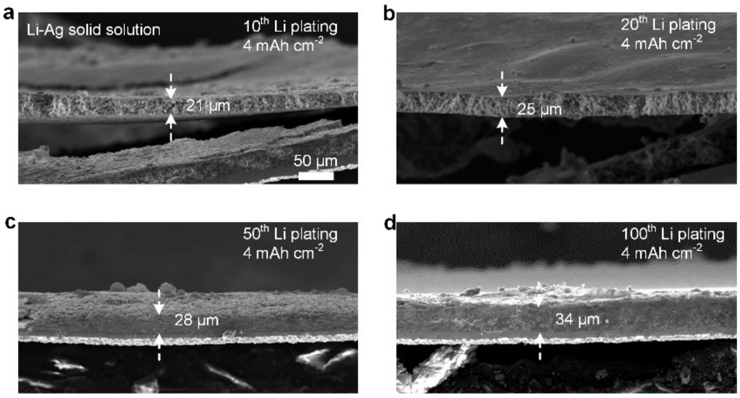

Figure S7. Cross-section SEM images of $Li_{12}Ag$ layers after (a) 10, (b) 20, (c) 50, and (d) 100 cycles at 1 mA cm^{-2} and 4 mAh cm^{-2}, respectively.

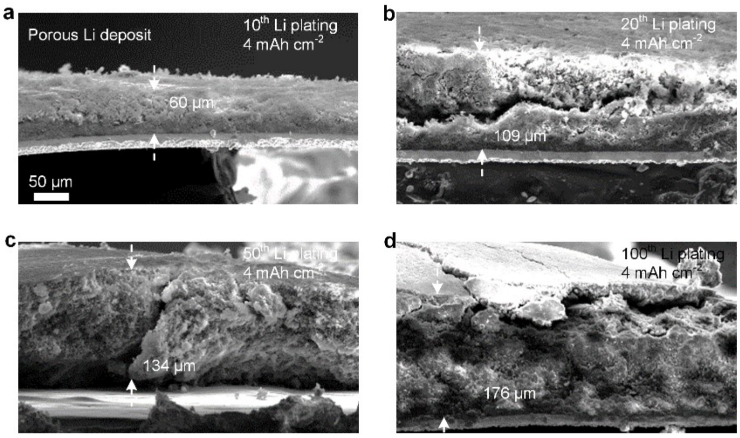

Figure S8. Cross-section SEM images of Li plating layers (4 mAh cm^{-2}) after (a) 10, (b) 20, (c) 50, and (d) 100 cycles at 1 mA cm^{-2} and 4 mAh cm^{-2}, respectively.

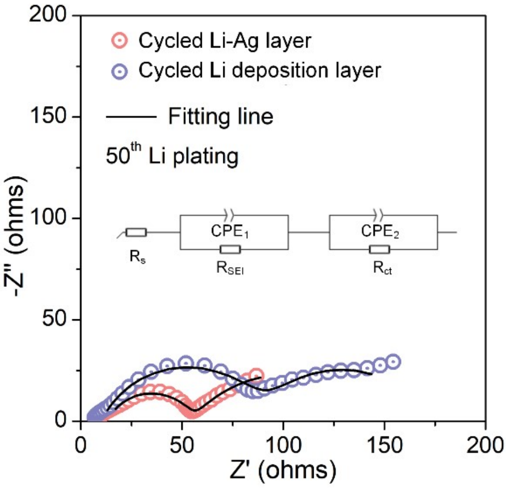

Figure S9. Nyquist points and the fitting lines of the $Li_{12}Ag$ and Li plating layers (4 mAh cm^{-2}) after 50 cycles at 1 mA cm^{-2} and 4 mAh cm^{-2}. R_s, R_{SEI}, and Rct represent the solution, SEI film, and charge transfer resistances, respectively. CPE_1, CPE_2 and CPE_3 correspond to constant phase elements.

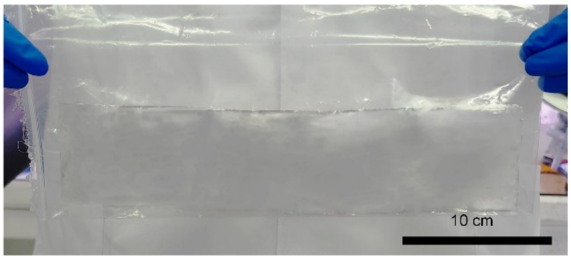

Figure S10. Digital image of Li/Ag anode with a size of 6.5 × 30 cm. The Li/Ag foil with a size of 6.5 × 30 cm could be easily produced using a facile roll-to-roll manufacturing process

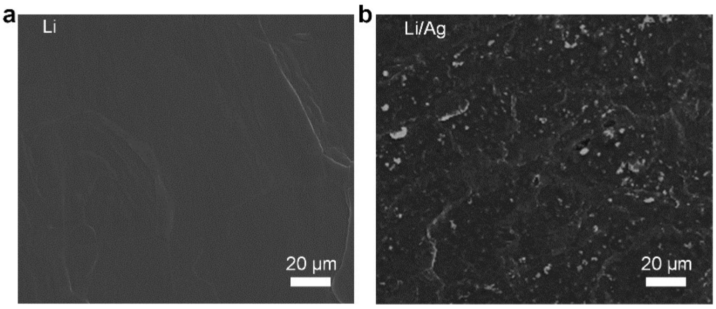

Figure S11. Top-view SEM images of (a) Li and (b) Li/Ag anode.

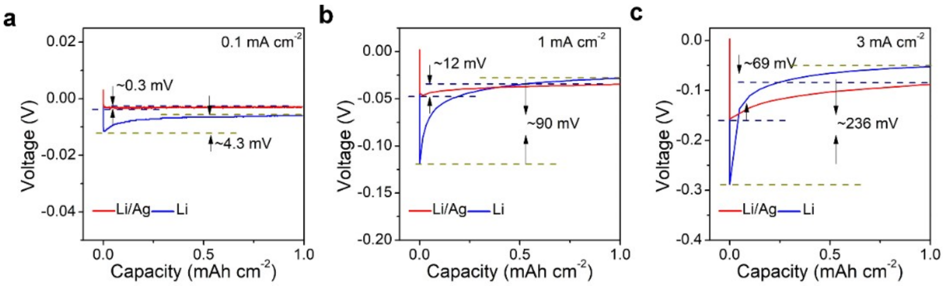

Figure S12. Li plating curves of Li and Li/Ag electrodes at (1) 0.1 (b) 1, and (c) 3 mA cm^{-2} with fixed capacity of 1 mAh cm^{-2}.

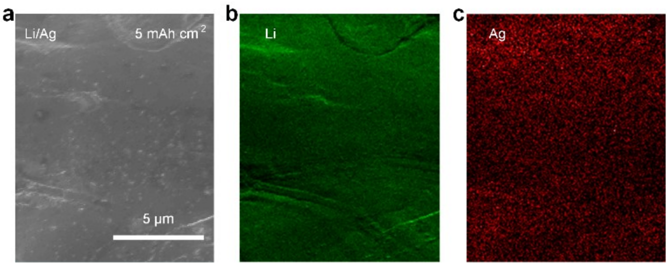

Figure S13. (a) SEM images and surficial AES mappings of (b) Li and (c) Ag elements for the Li/Ag electrode with the Li plating capacity of 5 mAh cm^{-2}.

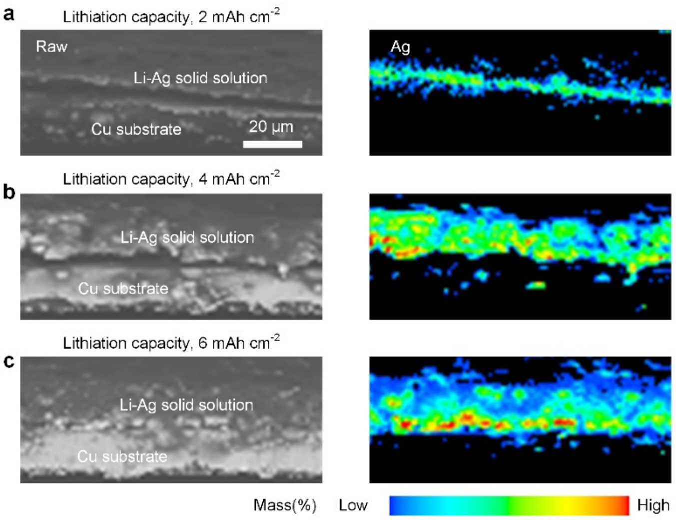

Figure S14. Backscattered electron (BSE) images of Ag electrode and the corresponding Ag element mapping images after Li filling for (a) 2, (b) 4, and (c) 6 mAh cm^{-2} detected by electron probe microanalysis (EPMA). The diffusion of Ag to the freshly plated Li was observed, demonstrating the Li-Ag solid solution formation via electrochemical lithiation processes

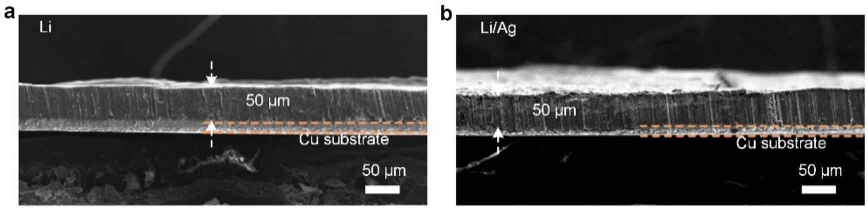

Figure S15. Cross-section SEM images of (a) Li foil and (b) Li/Ag foil. To facilitate characterization, the foils were rolled on a 18 μm-thick Cu substrate.

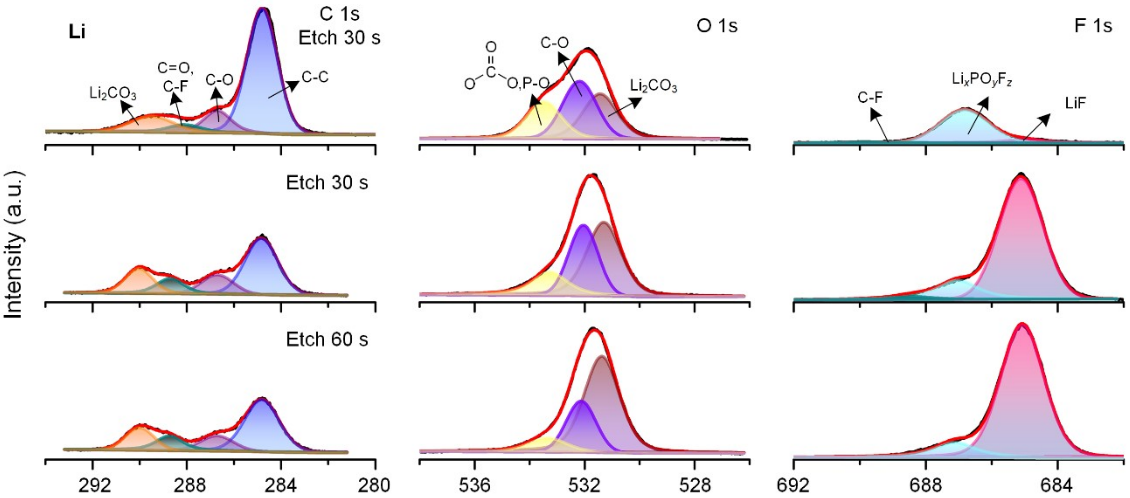

Figure S16. High-resolution C1s, O1s, and F1s XPS spectra before and after etching of Li-Ag layer.

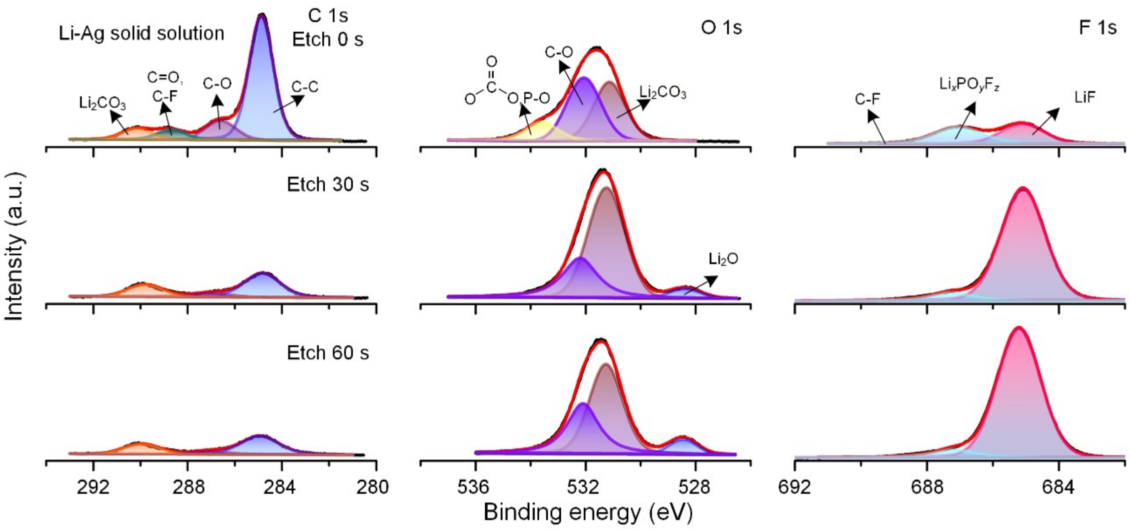

Figure S17. High-resolution C1s, O1s, and F1s XPS spectra before and after etching of Li plating layer.

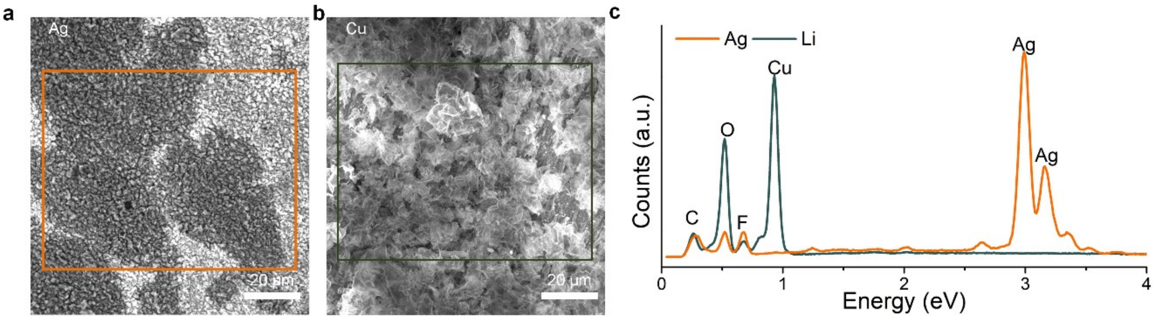

Figure S18. SEM images of (a) Li-Ag layer and (b) Li plating layer, (c) the corresponding EDS spectra corresponding to the selected regions in (a) and (b).

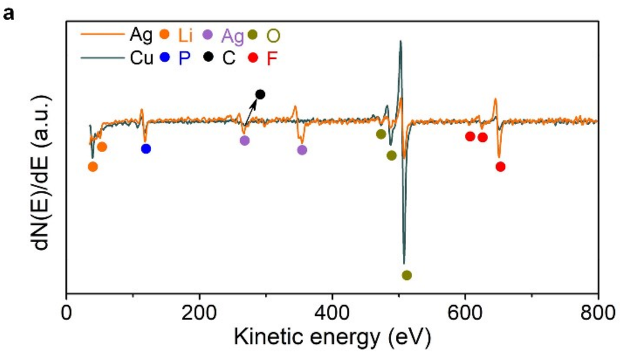

b

Elements	Kinetic energy (eV)
Li	31, 38, 49
P	120
Ag	262, 301, 351, 356
C	272
O	475, 490, 510
F	605, 625, 650

Figure S19. (a) Auger electron spectroscopy (AES) spectra of Li-Ag layer and Li plating layer, (b) the corresponding kinetic energy of different elements.

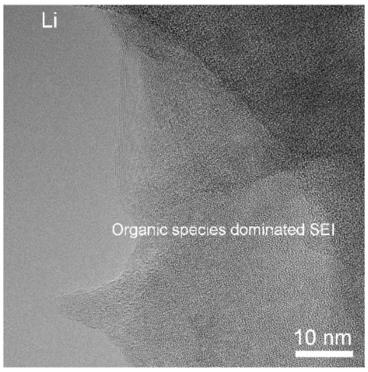

Figure S20. High-resolution transmission electron microscopy (HRTEM) image of the Li deposit.

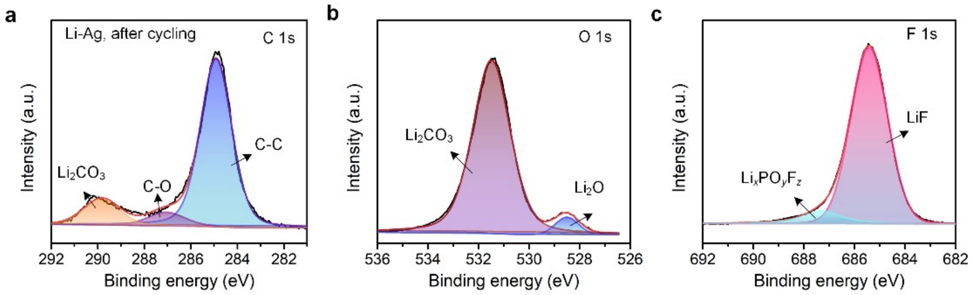

Figure S21. High-resolution (a) C 1s, (b) O 1s, and (c) F 1s XPS spectra of Li-Ag after 50 cycles after etching 30 s with Ar^+.

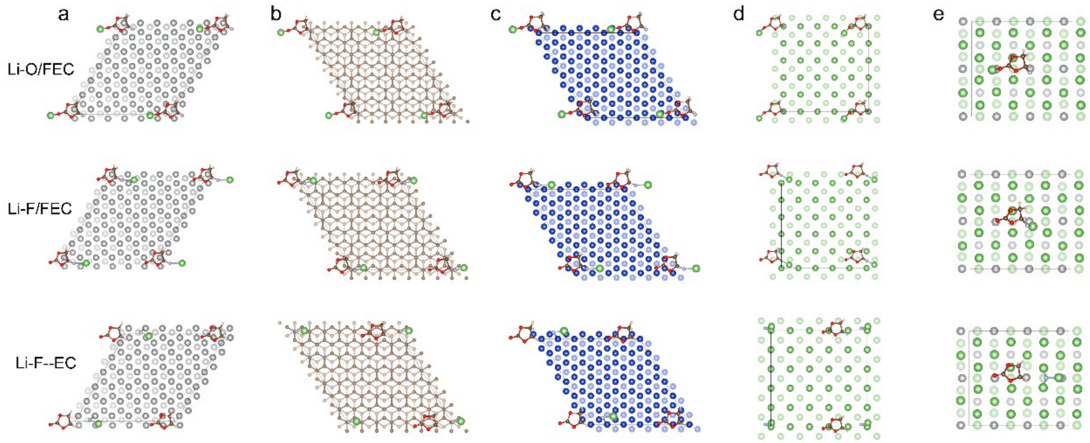

Figure S22. Atomic structures of Li$^+$-FEC species on (a) Ag (111), (b) graphite (001), (c) Cu (111), (d) Li (001), and (e) Li$_3$Ag (110).

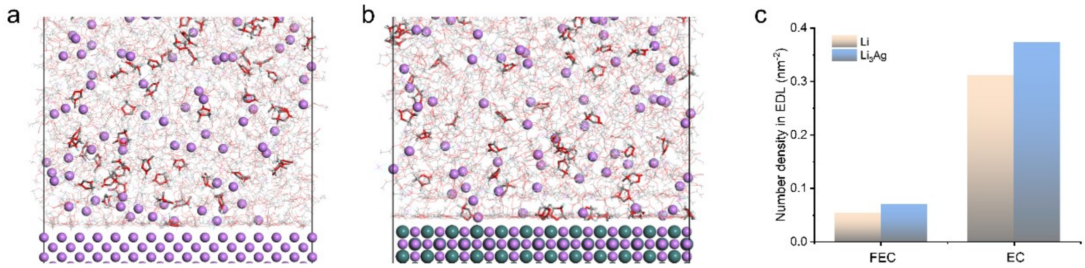

Figure S23. Atomic structures of QM/MM models for (a) Li and (b) Li_3Ag. (c) Corresponding Li^+ coordinated species number density in the electrical double layers.

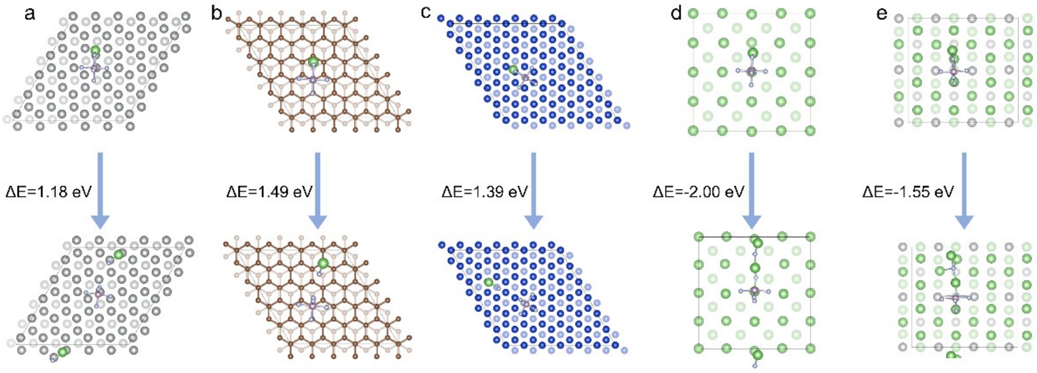

Figure S24. Atomic configurations and reaction energies of Li^+-PF_6^- species on (a) Ag (111), (b) graphite (001), (c) Cu (111), (d) Li (001), and (e) Li_3Ag (110).

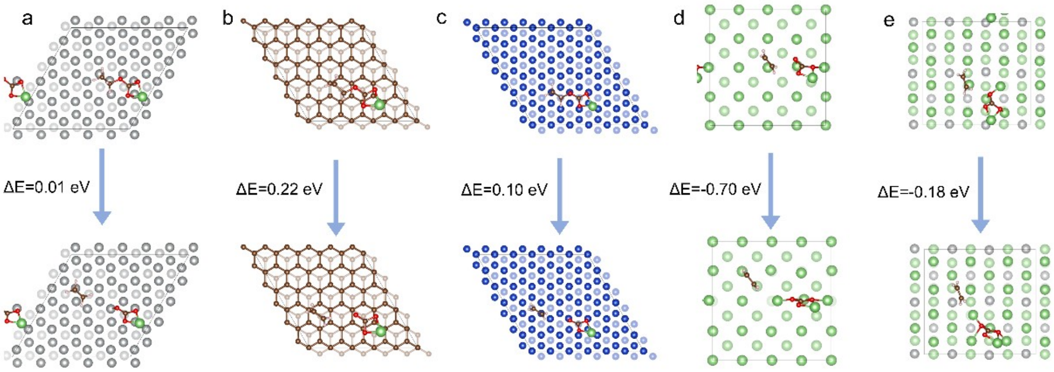

Figure S25. Atomic configurations and reaction energies of Li^+-EC species on (a) Ag (111), (b) graphite (001), (c) Cu (111), (d) Li (001), and (e) Li_3Ag (110).

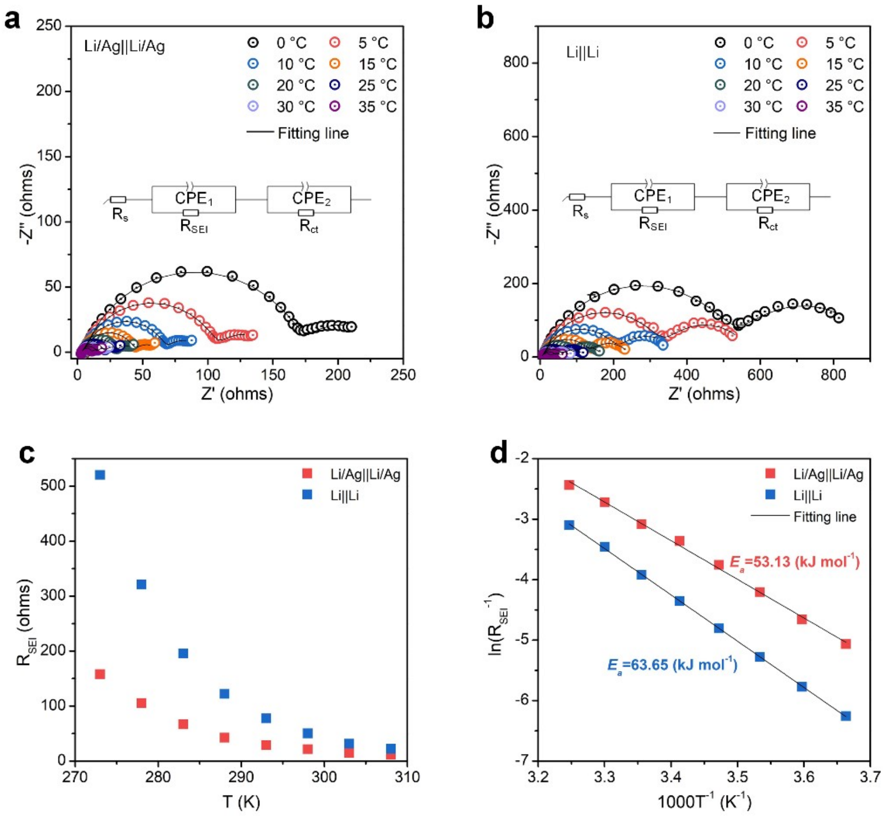

Figure S26. Nyquist points of (a) the Li/Ag||Li/Ag and (b) Li||Li cells tested at various temperatures ranging from 0 to 35 °C. The inserts were the equivalent circuit model. (c) Corresponding fitted R_{SEI} values of Li/Ag||Li/Ag and Li||Li. (d) Linearly fitting results of the relationship between $\ln(R_{SEI}^{-1})$ and T^{-1}. The relationship between R_{SEI} and E_a is described by Arrhenius' equation: $RSEI^{-1} = A \exp(-E_a/RT)$.

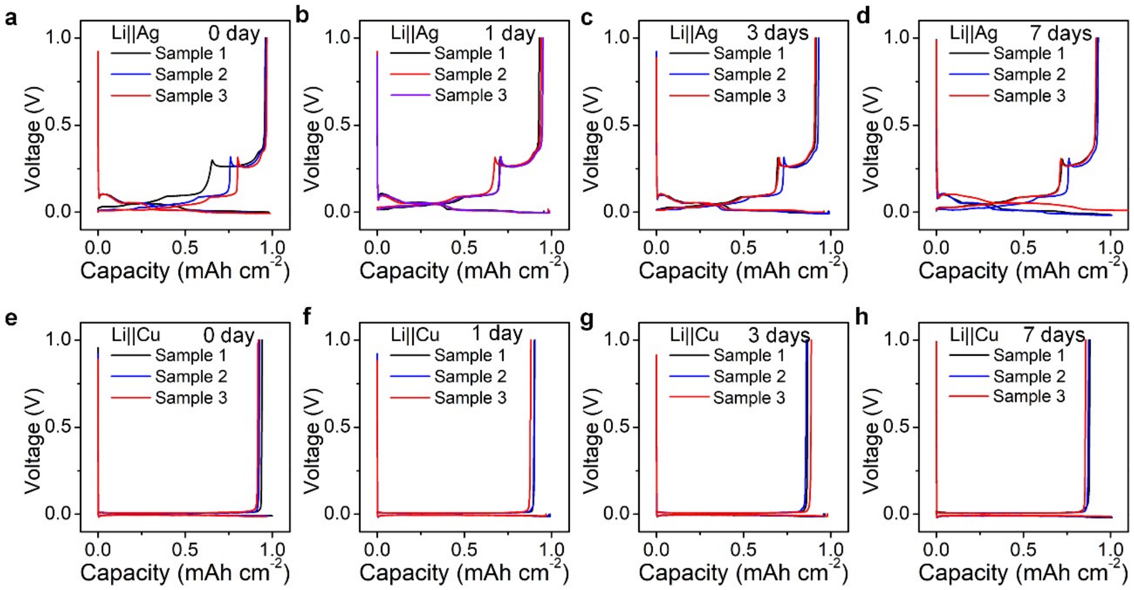

Figure S27. The 3rd discharge/charge curves of Li||Ag cells after aging for (a) 0, (b) 1, (c) 3, and (d) 7 days. The 3rd discharge/charge curves of Li||Cu cells after ageing for (e) 0, (f) 1, (g) 3, and (h) 7 days. These curves were corresponded to the result of Figure 4a.

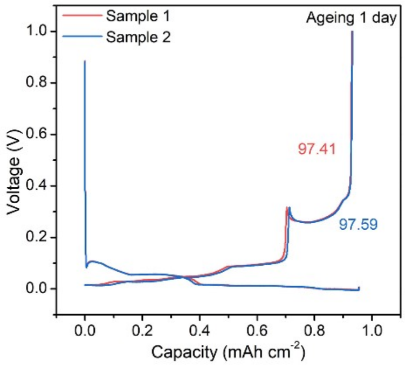

Figure S28. The discharge/charge curves of Li||Ag cells after aging for 1 day with an electrolyte of 10wt% FEC.

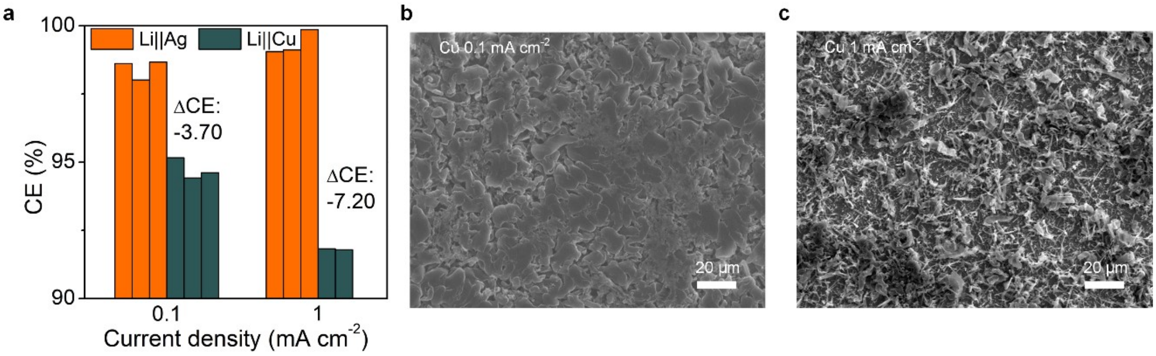

Figure S29. (a) Comparison of Colombic efficiency for the Li||Ag and Li||Cu cells with the current density of 0.1 and 1 mA cm^{-2}. Top-view SEM images of Li plating layers formed at (b) 0.1 and (c) 1 mA cm^{-2} with capacity of 1 mAh cm^{-2}.

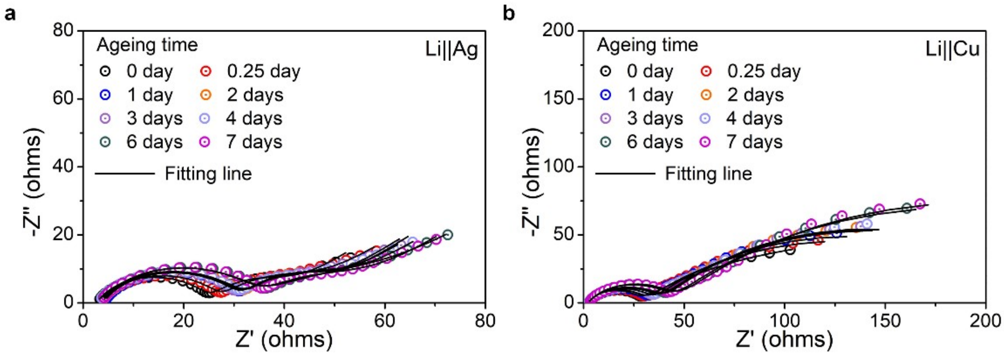

Figure S30. Nyquist points of (a) Li-Ag and (b) Li plating layers with different aging time.

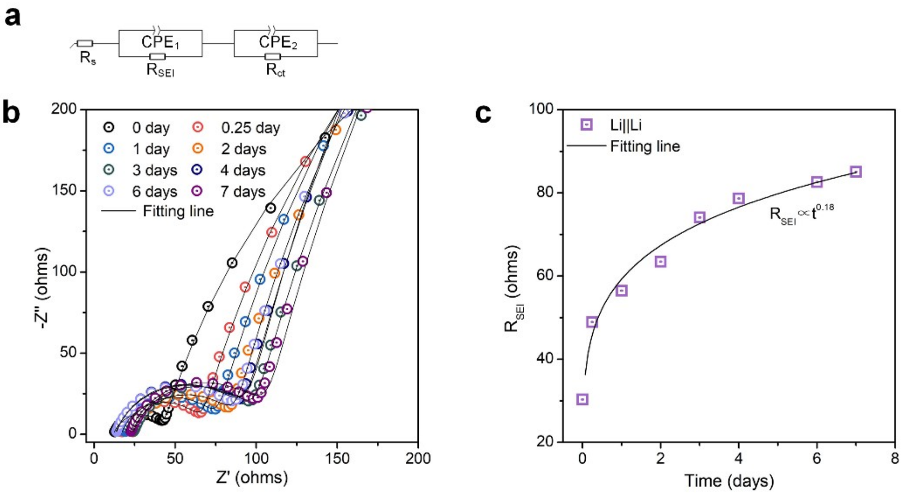

Figure S31. (a) The used equivalent circuit diagram of the fitted Nyquist points. (b) Nyquist points of Li/Li cell with different aging time. (c) R_{SEI} and the corresponding non-linear least squares fit to a power law.

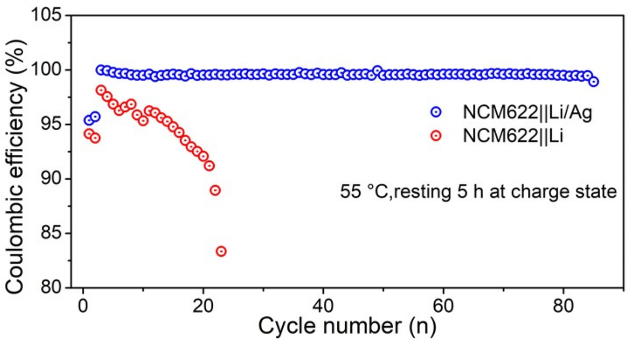

Figure S32. Cycle number-Coulombic efficiency points of the $LiNi_{0.6}Co_{0.2}Mn_{0.2}O_2$ (NCM622)||Li/Ag and NCM622||Li cells. The cells were aged under 55 °C for 5 hours at full charging state of each cycle.

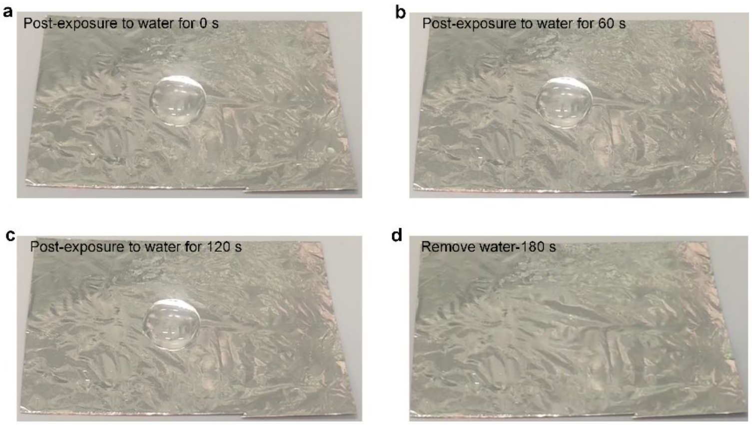

Figure S33. Digital images of the Li/Ag foil post-exposure to water for (a) 0, (b) 60, (c) 120 s, and (d) after removing water.

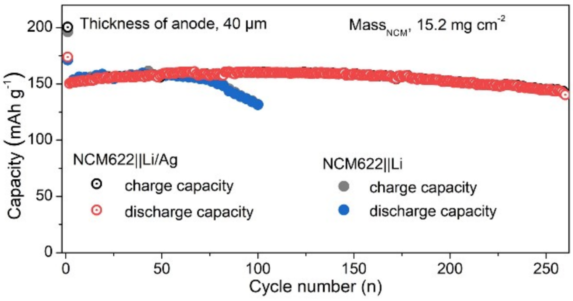

Figure S34. Cycling performance of the NCM622||Li/Ag and NCM622||Li coin cells. The cells was first cycled at 0.1 C (1 C = 175 mA g^{-1}) for activation, then cycled at 0.5 C.

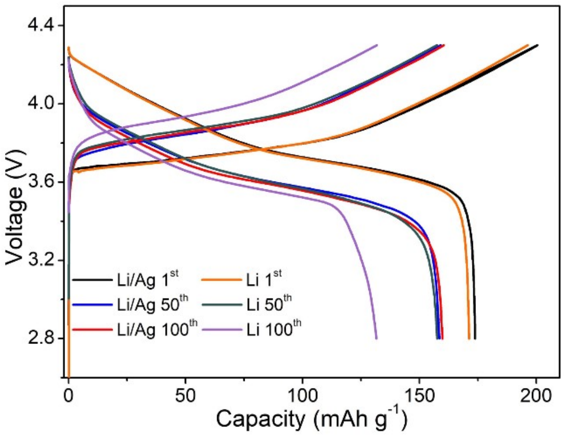

Figure S35. The voltage-capacity curves of the NCM622||Li/Ag and NCM622||Li coin cells at the 1st, 50th, and 100th cycles.

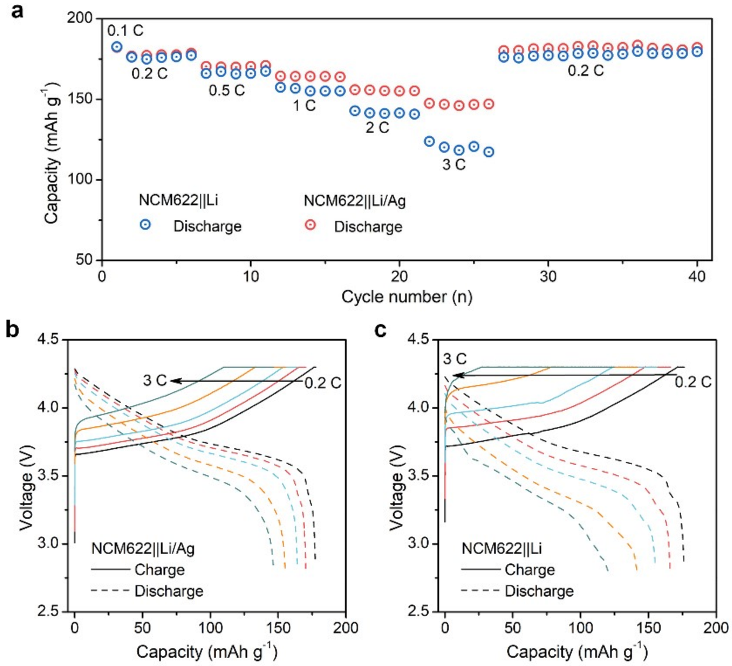

Figure S36. (a) Rate performance of NCM622||Li/Ag and NCM622||Li cells. (b) The corresponding charge/discharge curves of NCM622||Li/Ag and (c) NCM622||Li at 0.2 C (5th), 0.5 C (10th), 1 C (15th), 2 C (20th) and 3 C (25th).

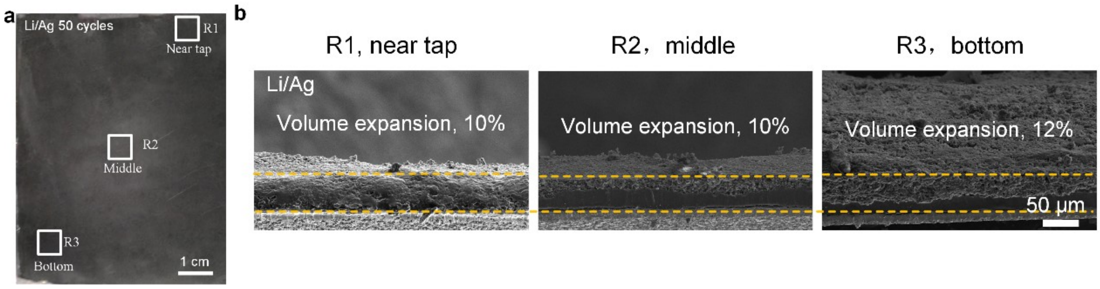

Figure S37. (a) Digital photos of the cycled Li/Ag anode and (b) the cross-section SEM images at different regions (near tap, the middle and bottom) at 1 mA cm^{-2} and 1 mAh cm^{-2}.

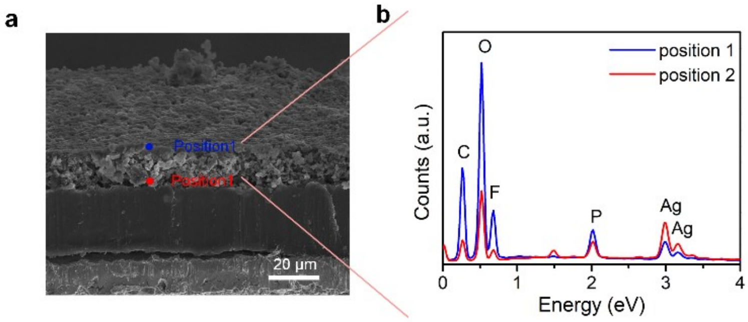

Figure S38. (a) Cross-section SEM images and the location for element analysis of the Li/Ag electrode after 50 cycles, and (b) the corresponding EDX spectra.

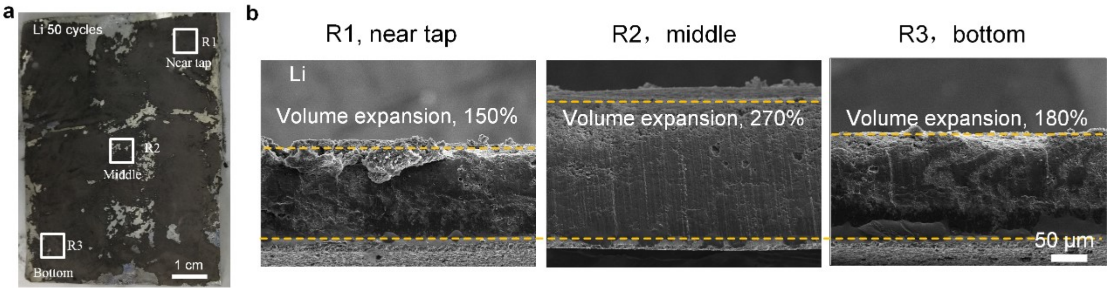

Figure S39. (a) Digital photos of the cycled Li anode and (g) the corresponding cross-section SEM images at different regions (near tap, the middle and bottom) at 1 mA cm^{-2} and 1 mAh cm^{-2}.

Figures S37-39 depict the SEM observations of the cycled Li/Ag and pure Li electrodes in a pouch cell configuration at 1 mA cm^{-2} and 1 mAh cm^{-2} after 50 cycles. The Li/Ag electrode exhibited a flat and uniform surface, devoid of any Li exfoliation (**Figure S37**a). The volume expansion ratios of the cycled Li/Ag anode were approximately 10% at various selected regions within an electrode of dimensions 6 × 8 cm (near the tap, middle, and bottom), further corroborating the suppressed volume expansion and excellent uniformity of the electrochemical reaction on the Li/Ag anode (**Figure S37b**). Energy-dispersive X-ray (EDX) spectroscopy analysis of the cycled Li/Ag anode revealed that the Ag signal was confined to a variable depth within the surface reaction layer, suggesting that the electrochemical reaction was limited to the initial Ag layer (**Figure S38**). Conversely, digital images of the cycled pure Li anode displayed a loosely structured surface, with severe exfoliation evident on the loosely adhered electrode surface (**Figure S39a**). Moreover, substantial volume expansion with significant fluctuation was observed on the cycled Li electrode, with values of 150%, 270%, and 180% in the selected areas, respectively (**Figures S39b**).

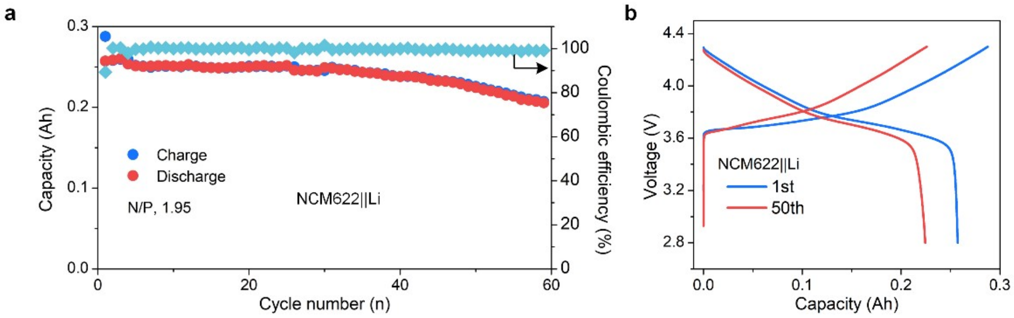

Figure S40. (a) Cycling performance of the 0.25 Ah NCM622||Li pouch cell (0.2 C charge/discharge), and (b) the corresponding voltage-capacity curves at the 1st and 50th cycles.

Table S1. Data sources of the density and lithiation/delithiation potential of various Li-containing materials.

Materials	Density (g cm^{-3})	Li density (g cm^{-3})	Average potential (V)
Li_3Sb	3.36 (JCPDS#89-4221)	0.49	~0.95 (ref.3)
Li_3Bi	5.02 (JCPDS#27-0427)	0.46	~0.82 (ref.4)
Li_2Ga	2.92 (JCPDS#83-1228)	0.49	~0.45 (ref.5)
$Li_{22}Sn_5$	1.92 (JCPDS#18-0753)	0.39	~0.50 (ref.3)
Li_9Al_4	1.27 (JCPDS#24-0008)	0.47	~0.47 (ref.6)
LiZn	4.18 (JCPDS#03-0954)	0.4	~0.38 (ref.4)
$Li_{22}Si_5$	1.01 (JCPDS#65-3134)	0.52	~0.35 (ref.7)
$Li_{13}In_3$	2.29 (JCPDS#33-0615)	0.48	~0.30 (ref.8)
LiAg	5.96 (JCPDS#04-0805)	0.36	~0 (ref.9)
$Li_{3.3}Ag$	2.66 (JCPDS#02-1097)	0.47	~0 (ref.9)
$Li_{6.46}Mg$	0.74 (JCPDS#09-0215)	0.48	~0 (ref.9)
Li	0.53 (JCPDS#89-3940)	0.53	~0 (ref.10)

Li density is obtained by multiplying the density of different materials by the proportion of Li in the total mass.

Table S2. Li density of various Li_xAg solid solution

Three electrodes were used to calculate the average value of the parameters. Area of each tested electrode was fixed as 0.5 cm^2. Density of the Li-Ag solid solutions is obtained by dividing mass by volume, and the corresponding Li density is obtained by multiplying the density by the proportion of Li in the total mass.

Electrodes	Average thickness (mm)	Average mass (mg)	Density (g cm^{-3})	Li density (g cm^{-3})
Pure Li	0.5	13.31	0.532	0.532
Li_6Ag	0.5	44.23	1.769	0.492
Li_9Ag	0.5	35.52	1.421	0.521
$Li_{12}Ag$	0.5	31.05	1.242	0.541
$Li_{15}Ag$	0.5	28.04	1.122	0.551
$Li_{18}Ag$	0.5	24.81	0.992	0.532

Table S3. Fitting parameters for RSEI.
R_{SEI} was fitted to a power law ($R_{SEI} \propto at^x$)

Electrodes	a	x
Li-Ag solid solution	26.5 ± 0.17	0.8 ± 0.004
Plated Li	31.7 ± 0.51	0.14 ± 0.011

Table S4. The specifications of the 2.45Ah NCM622||Li/Ag pouch cell.

Components	Specification	Value
Cathode (NCM622) 7.8 × 7.8 cm	mass loading of active material for each side (mg cm^{-2})	23.2
	Active material content	0.95
	Number of electrodes	10
	Number of Al current collector	6
	Mass of Al current collector (g)	0.059
	Total weight of cathode (g)	14.9
Anode (Li/Ag foil)	Thickness of Li (two sides, μm)	80
	Thickness of Ag (μm)	1.3
	Number of Ag	10
	Number of Li	5
	Total weight of anode (g)	2.1
Electrolyte	Electrolyte/capacity (g Ah^{-1})	1.71 (3.5 ml)
	Weight (g)	4.2
Separator (PP)	Weight (g)	0.6
Pouch cell	N/P	1.95
	Discharge capacity (Ah)	2.45
	Mid-value voltage (V)	3.748
	Discharge energy (Wh)	9.183
	Total weight (g)	21.8
	Specific energy (Wh kg^{-1})	421

Reference

1 W. S. L D Firth, N H A Nowaina, *J. Phys. F: Met. Phys.* 1974, **4**, L200.

2 D. L. S H Kellington, J M Titman, *J. Phys. D: Appl. Phys.* 1969, **2**, 1162.

3 N. Liang, H. Xu, H. Fan, Z. Li and S. Li, *ACS Appl. Mater. Interfaces* 2022, **14**, 13326-13334.

4 M. N. Obrovac, V. L. Chevrier, *Chem. Rev.* 2014, **114**, 11444-11502.

5 C. Wei, L. Tan, Y. Zhang, Z. Wang, B. Xi, S. Xiong, J. Feng and Y. Qian, *Energy Storage Mater.* 2022, **50**, 473-494.

6 J. Sun, Q. Zeng, R. Lv, W. Lv, Q. Yang, R. Amal and D.-W. Wang, *Energy Storage Mater.* 2018, **15**, 209-217.

7 J. Zhao, Z. Lu, H. Wang, W. Liu, H. W. Lee, K. Yan, D. Zhuo, D. Lin, N. Liu and Y. Cui, *J. Am. Chem. Soc.* 2015, **137**, 8372-8375.

8 S. A. Webb, L. Baggetto, C. A. Bridges and G. M. Veith, *Journal of Power Sources* 2014, **248**, 1105-1117.

9 B. T. Heligman, A. Manthiram, *ACS Energy Lett.* 2021, **6**, 2666-2672.

10 K. Yan, Z. Lu, H.-W. Lee, F. Xiong, P.-C. Hsu, Y. Li, J. Zhao, S. Chu and Y. Cui, *Nat. Energy* 2016, **1**, 16010.